



# Enhanced Photocatalytic Performance of Zinc Ferrite Nanocomposites for Degrading Methylene Blue: Effect of Nickel Doping Concentration

Jannat Hammouche<sup>1,2</sup> · M. Gaidi<sup>3,4,5</sup> · S. Columbus<sup>5</sup> · M. Omari<sup>2</sup>

Received: 15 January 2021 / Accepted: 2 March 2021 / Published online: 7 April 2021

© The Author(s), under exclusive licence to Springer Science+Business Media, LLC, part of Springer Nature 2021

## Abstract

In the present work, undoped and nickel doped zinc ferrite ( $ZnFe_{2-x}Ni_xO_4$ ) nano-composites were synthesized using a facile auto-combustion method using glycine as fuel. Effects of Ni dopant concentration and annealing process on structural and morphological properties were investigated by X-ray Diffraction (XRD), Raman spectroscopy, Fourier Transform InfraRed (FTIR) spectroscopy, and Scanning Electron Microscopy/Energy-dispersive X-ray spectroscopy (SEM/EDS). The formation of cubic spinel ferrites is confirmed by XRD analysis while asserting particles with a size range of 55–58 nm. Analysis of Raman spectra showed a transition of normal to inverse spinel-type with the increase in Ni content. Photocatalytic studies of as-synthesized nanoparticles using methylene blue (MB) demonstrated a strong correlation between photocatalytic efficiency and Ni doping. Ni-doped zinc-ferrites exhibited 98% photocatalytic efficiency at an optimum Ni doping concentration of 30%. As-synthesized ferrites have the potential to be used as an efficient, reusable, and magnetically removable photocatalyst system for removing organic pollutants.

**Keywords** Zinc ferrite · Nanosized oxides · Auto-combustion · Photocatalysis · Methylene blue

## 1 Introduction

The immense exploitation of synthetic organic compounds for diverse industrial processes often created drastic environmental pollution worldwide [1]. Discharge of wastewater from large-scale industries is found to contain organic dye remnants which are reported to be extremely devastating to the entire ecosystem. Methylene blue (MB) is a typical

aromatic dye that is usually employed in textile industries for the dyeing process of silk and cotton materials [2, 3]. Being stable, toxic, and non-degradable, these dye fractions even at low trace levels can deteriorate the quality of water significantly [4]. On potential exposure, human health could be endangered by its inherent carcinogenicity and tissue necrotic effects [5]. Besides, the photosynthesis of aquatic organisms could be hindered by the stable coloured nature of dye molecules. Extensive efforts based on adsorption, filtration, ion exchange, and chlorination have been put forward for addressing water remediation [6–8]. The development of advanced remediation strategies remains one of the global concerns owing to the increased threat of water contamination [9]. In this scenario, photocatalysis has acquired immense research attention where the organic contaminants can be completely degraded to nontoxic end products in an eco-friendly manner [10–13]. Besides, the formation of secondary toxic by products can be avoided by this technique. In addition to frequently employed photocatalysts based on titanium dioxide and zinc oxide, other systems like strontium/cerium bimetallic nanocomposites, pectin zirconium (IV) selenotungstophosphate nanocomposites are reported to be highly effective under ultra-violet or visible light sources [14, 15]. Still, different strategies have been put forward to

✉ Jannat Hammouche  
hammouche-djennat@univ-eloued.dz

<sup>1</sup> Department of Exact Sciences, University of El-Oued Echahid Hamma Lakhdar, 39000 El-Oued, Algeria

<sup>2</sup> Laboratory of Molecular Chemistry and Environment, University of Biskra Mohamed Khider, 07000 Biskra, Algeria

<sup>3</sup> Department of Applied Physics and Astronomy, University of Sharjah, PO Box 27272, Sharjah, UAE

<sup>4</sup> Centre for Advanced Materials Research, Research Institute of Sciences and Engineering, University of Sharjah, P. O. Box 27272, Sharjah, United Arab Emirates

<sup>5</sup> Laboratoire de Photovoltaïque, Centre de Recherches et des Technologies de l'Énergie, Technopole de Borj-Cédria, BP 95, 2050 Hammam-Lif, Tunisia

address challenges such as achieving high efficiency, ease of recoverability and ability of sunlight driven catalysis.

Magnetic zinc ferrites ( $\text{ZnFe}_2\text{O}_4$  or ZFO) are attracted enormous research attraction owing to their unique electric, magnetic and catalytic properties; while exhibiting high stability and ease of fabrication with reproducibility [16, 17]. These are n-type semiconductors with cubic structure and frequently used for various electronic applications [18–20]. Besides, these are characterized by a low bandgap of  $\sim 1.9$  eV as determined in the work of Jang et al. and Borse et al. by using UV–Visible Diffuse Reflectance Spectroscopy (UV–Vis DRS), also characterized by a well suited electronic structure and broad absorption in the visible range making it suitable for many water redox reactions [21, 22]. Ferrite nanocomposites can be synthesized by various techniques such as hydrothermal, sonochemical, co-precipitation, and sol–gel auto combustion [23–27]. Among them, auto-combustion methods are mostly favourable owing to the simplicity, versatility, rapid completeness of reaction, the homogeneous addition of dopant could be ensured [28]. During the process, metal nitrates can be homogeneously mixed in presence of fuel materials like hydrazides, urea, glycine, and citric acid. Magnetic recoverable ferrite composite was found to be quite appealing in the photocatalysis process as easy and complete separation of catalyst from the rest of the medium is possible using an external magnet. While conventional photocatalysts require mostly centrifugation or filtration for further removal, the catalyst recovery rate, and reusability could be much enhanced in the case of ferrites [29–31]. Besides, high surface area to volume ratio and quantum confinements of nano ferrites is most promising to get high efficient photocatalysts.

Recently studies have been reported on catalytic aspects of ZFO composites as the morphology and structural parameters can influence their performance. Nevertheless, few endeavours have investigated nickel–zinc ferrite nanocomposites materials for photocatalytic purposes. In the current work, ZFO samples were prepared by the auto-combustion method and annealed at  $1000^\circ\text{C}$ . The effect of Ni dopant concentration on ZFO structure and morphology was studied in detail. It was found that doped samples present pure crystallographic and high efficiency regarding methylene blue decomposition.

## 2 Experimental

### 2.1 Materials

Base materials such as zinc nitrate ( $\text{Zn}(\text{NO}_3)_2 \cdot 6\text{H}_2\text{O}$ ), ferric nitrate ( $\text{Fe}(\text{NO}_3)_3 \cdot 9\text{H}_2\text{O}$ ), nickel nitrate ( $\text{Ni}(\text{NO}_3)_2 \cdot 6\text{H}_2\text{O}$ ),

glycine ( $\text{C}_2\text{H}_5\text{NO}_2$ ) from Sigma Aldrich, USA, and methylene blue from IBA scientific, IA were used for the present study.

### 2.2 Synthesis and Characterization of Zinc Ferrites

ZFO samples were prepared by dissolving and mixing the nitrates of Zinc, Iron, and nickel as precursors and glycine as fuel. Formation of the homogenous gel was ensured by applying stirring at  $80^\circ\text{C}$  which finally undergone combustion [32]. The flame temperature during combustion can be from  $600$  to  $1350^\circ\text{C}$ . After burning in the air and grinding, the burned gel turned to powder. All samples have then been annealed at  $1000^\circ\text{C}$  under air. The Ni content in the  $\text{ZnFe}_{2-x}\text{Ni}_x\text{O}_4$  prepared samples was changed from  $x=0.05$  to  $0.4$  in weight percentage in the starting solutions.

The annealed samples were characterized by an X-Ray diffractometer (D8 advanced Bruker), Raman spectroscopy (RENISHAW) with laser edge  $785$  nm, FTIR (JASCO FT/IR-6300), Field Emission SEM/EDS (Thermo scientific Apreo C).

### 2.3 Photocatalytic Studies

The photocatalytic activity of as-prepared samples was evaluated using a photochemical reactor (Techinstro, India) equipped with a  $450$  W ultraviolet (UV) lamp. For this,  $300$  ml aqueous solution of methylene blue ( $0.02 \times 10^{-3}$  mol/L) was taken in the reaction vessel followed by the addition of  $0.1$  g of ZFO doped by Ni ( $x=0, 0.05, 0.15, 0.3,$  and  $0.4$ ). Adsorption–desorption equilibrium of dye on the photocatalyst surface was ensured by magnetic stirring in dark for  $20$  min. The reaction medium is then subjected to UV light and the temperature was kept steady during the reaction using an external water circulatory chiller unit. The decrease in absorption values of MB solutions was continuously monitored at each  $20$  min time interval using a UV–Visible spectrophotometer [33]. The degradation efficiency is calculated using the following equation:

$$\text{Degradation of dye (\%)} = \left[ \frac{(C_0 - C_t)}{C_0} \right] \times 100\% \quad (1)$$

$$= \left[ \frac{(A_0 - A_t)}{A_0} \right] \times 100\% \quad (2)$$

where  $C_0$  and  $C_t$  are the initial and the final concentrations, respectively;  $A_0$  and  $A_t$  are the corresponding absorbance values of MB, which were measured at the highest absorbance peak of MB of  $665$  nm.

### 3 Results and Discussion

#### 3.1 Structural Characterization

ZFO nanocomposites were successfully synthesized by auto-combustion method by varying the Ni content from 5 to 40% of  $\text{ZnFe}_{2-x}\text{Ni}_x\text{O}_4$  ( $x=0, 0.05, 0.15, 0.3$  and  $0.4$ ). The diffractograms of the synthesized samples were annealed at  $1000^\circ\text{C}$  (Fig. 1a). The XRD spectra were analyzed by X'Pert high score software to check their structure allowed us according to find that the diffraction peaks of sample  $x=0$  are in good agreement with the ASTM card No. (01-073-1963) of pure Zinc Ferrite cubic phase

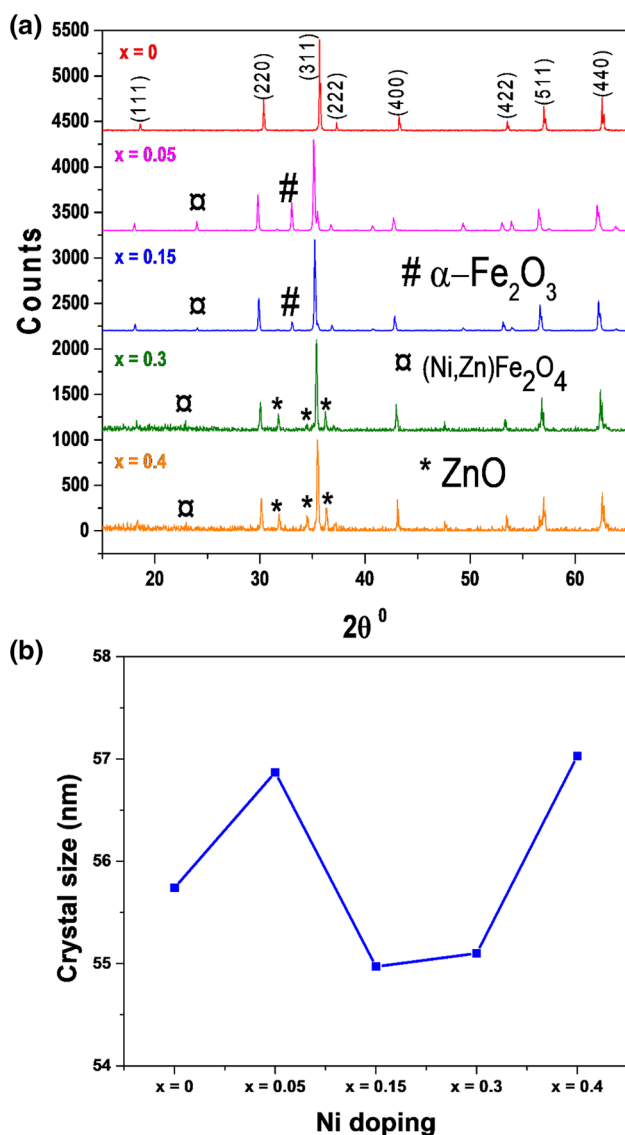


**Fig. 1** a XRD pattern of  $\text{ZnFe}_{2-x}\text{Ni}_x\text{O}_4$  powder as a function of Ni doping ( $x=0.05, 0.15, 0.3$  and  $0.4$ ) after annealing at  $1000^\circ\text{C}$  under air and b Plot of crystal size versus Ni dopant concentration

with space group Fd3m which proves that the non-doped sample has a pure phase. The doped samples with  $x=0.05, 0.15, 0.3$  and  $0.4$  are in a good agreement with the ASTM card No. (01-073-1963) of pure Zinc Ferrite cubic phase with space group Fd3m. Extra peaks of secondary phases have been also observed [34]:

- For:  $x=0.05$  and  $0.15$  the indexation of extra peaks consistent with ASTM card No. (00-008-0234) of Nickel Zinc Iron Oxide  $(\text{Ni,Zn})\text{Fe}_2\text{O}_4$  cubic phase with space group Fd3m as and ASTM card No. (01-073-0603) of  $\alpha\text{-Fe}_2\text{O}_3$  (hematite) rhombohedral nanoparticles.
- For samples doped with  $x=0.3$  and  $0.4$  the extra phases fits with the ASTM card No. (00-008-0234) of Nickel Zinc Iron Oxide  $(\text{Ni,Zn})\text{Fe}_2\text{O}_4$  cubic phase with space group Fd3m as ZFO and ASTM card No. (00-001-1136) of ZnO hexagonal wurtzite nanoparticles.

The average crystallite size of zinc ferrites compositions was calculated from the XRD spectra using the Debye–Scherrer formula on the main peak (311) for all samples [35, 36]

$$D = \frac{0.9\lambda}{\beta \cos \theta} \quad (3)$$

where  $D$  is the crystalline size,  $\lambda$  denotes the wavelength of Cu-K $\alpha$  X-ray radiation,  $\beta$  is the full width at half maximum of XRD peaks and  $\theta$  is Bragg's angle. The variation of the crystal size of ZFO compositions was plotted as a function of Ni dopant concentration as shown in Fig. 1b. It can be seen that subsequent changes in Ni content impose a slight variation of crystal sizes from 55 to 57 nm. While lower and higher doping concentrations (5% and 40% respectively) resulted in slightly higher crystal size, the lowest crystal size was obtained for moderate Ni doping levels of 15 to 30%.

The characteristic Raman spectra of synthesized ZFO samples were represented in Fig. 2. It was reported that the positions of the peaks, Raman lines features, widths, energies, shape, and intensities get affected by the substitution leading to the changes in the lattice parameters and the cations positions in the lattice. The Raman shifts shows 5 modes ( $A_{1g} + E_g + 3F_{2g}$ ) as normal spinel for samples with  $x=0, 0.05$  and  $0.15$  type and inverse spinel-type for  $x=0.3$  and  $x=0.4$  ones due to  $A_{1g}$  mode represented as doublet peaks [37].

FTIR spectra of the synthesized ZFO samples were depicted in Fig. 3. Ferrites spinel oxides are reported to consist of two metal–oxygen (M–O) vibrations within the  $350\text{--}600\text{ cm}^{-1}$  range. The characteristic absorption peaks are observed between  $542$  and  $549\text{ cm}^{-1}$  due to

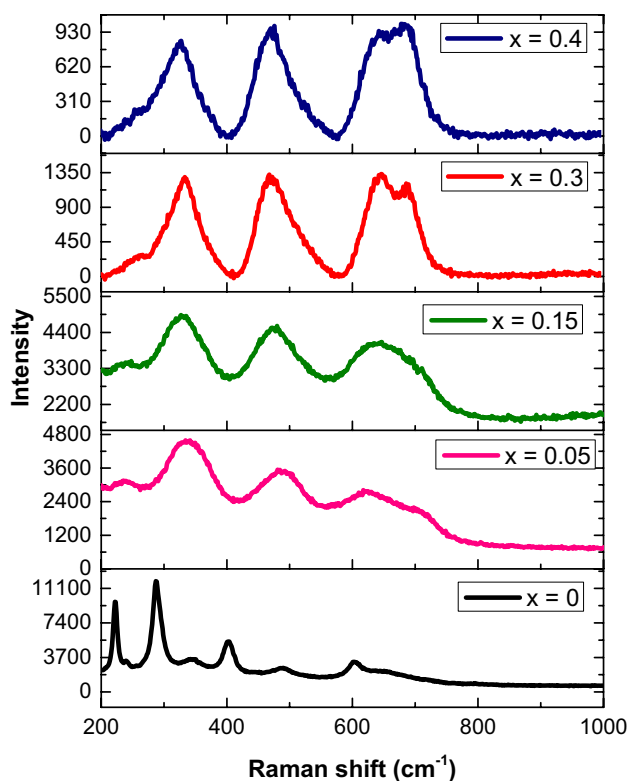


**Fig. 2** Effect of Ni content ( $x=0, 0.05, 0.15, 0.3$  and  $0.4$ ) on the Raman spectra of the  $\text{ZnFe}_{2-x}\text{Ni}_x\text{O}_4$  composites annealed at  $1000\text{ }^\circ\text{C}$  under air. Raman spectra acquired using  $785\text{ nm}$  laser,  $50\text{ mW}$  power, and  $10\text{ s}$  integration time

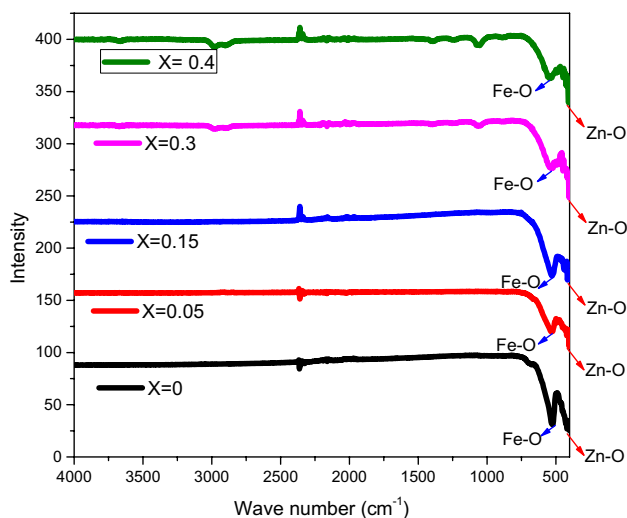


**Fig. 3** FTIR spectra of  $\text{ZnFe}_{2-x}\text{Ni}_x\text{O}_4$  with varying Ni content ( $x=0, 0.05, 0.15, 0.3$  and  $0.4$ ) after annealing at  $1000\text{ }^\circ\text{C}$

the stretching vibrations of the Fe–O bonds in octahedral positions [38, 39]. Furthermore, the characteristic peaks observed between  $401$  and  $415\text{ cm}^{-1}$  are due to

the stretching vibrations of the Zn–O bonds in tetrahedral positions [40, 41]. The peak around  $2900\text{ cm}^{-1}$  is not prominent still present in ZFO compositions; which represents C–H stretching vibrations. The absence of a peak around  $3000\text{ cm}^{-1}$  indicates the absence of water moieties, mostly due to the annealing process. Further, the peak near  $2300\text{ cm}^{-1}$  is mainly due to carbon dioxide molecules that adsorbed on the substrates.

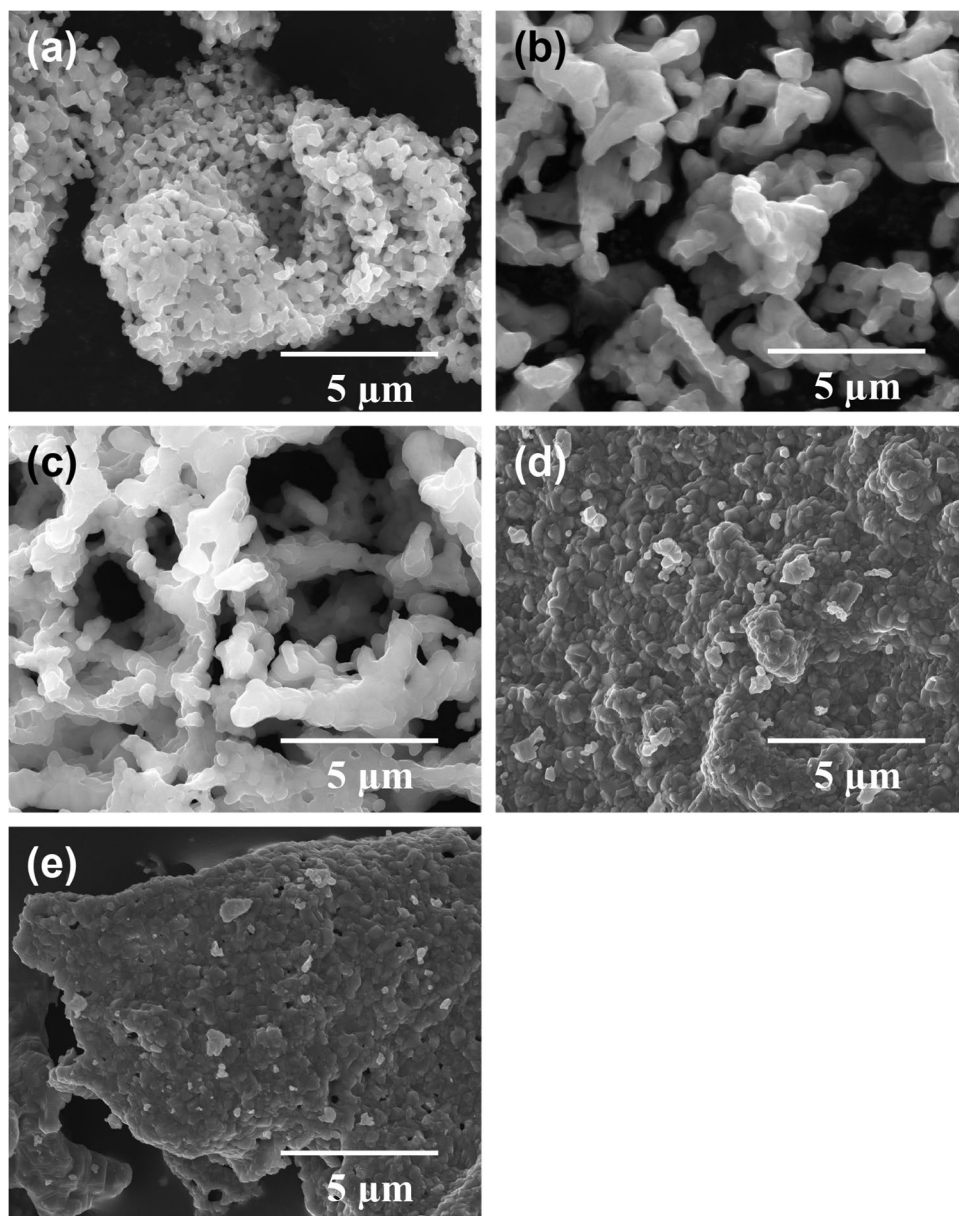
### 3.2 Morphological Analysis

The SEM micrographs of ZFO samples showed surface morphology of as-prepared samples (Fig. 4). The grain size was found to be in the range of  $103.5\text{--}652.5\text{ nm}$  for different compositions. Moreover, it could be noted that the particle size gets increased on the initial addition of Ni from 5 to 15%, thereafter it decreases. Some extent of agglomeration has clearly appeared in all compositions which might be attributed due to the exposure to higher temperatures during auto-combustion and annealing processes. The high surface area to volume ratio and inherent magnetic properties of nanoparticles can further facilitate the tendency for agglomeration. Our observation sounds well with previous studies conducted by Naik et al. for green synthesis of zinc ferrite nanoparticles using *Limonia acidissima* juice [42]. Moreover, the elemental analysis showed that as-synthesized zinc ferrites are composed of expected constituent elements such as Zn, Fe, O, and Ni [43]. This proved that the auto-combustion process produces pure zinc ferrites without any impurities (Fig. 5) where it represented the EDX of the pure ZFO and the Ni 30% doped one to check the Ni concentration.

### 3.3 Photocatalytic Activity

The photocatalytic behaviour of as-synthesized ZFO composites was investigated using methylene blue under UV light. The absorbance of MB subsequently decreased with increased during the reaction (Fig. 6a). It could be clearly seen that the photocatalytic performance of ZFO nanocomposites enhanced successively with Ni dopant up to 30% and thereafter decreases by 40% (Fig. 6b, c). After 200 min reaction, the degradation efficiencies of different composites were calculated and correlated with their corresponding crystal size (Fig. 7a). While bare ZFO exhibits  $\sim 95\%$  degradation of MB, zinc ferrite composite with 30% Ni dopant was found to have the highest degradation efficiency of  $\sim 98\%$ . Moreover, the rate constant of the reaction was also calculated for each nanocomposite as given in Fig. 7b. The highest rate constant of  $2.38 \times 10^{-2}$  was observed at 30% Ni content. The photocatalytic efficiency is then strongly correlated to the crystal size of nanocomposites. As the size is decreasing the specific surface area is increasing leading to a more exposed surface for dye adsorption. Besides,

**Fig. 4** FESEM images of  $\text{ZnFe}_{2-x}\text{Ni}_x\text{O}_4$  samples containing **a** 0, **b** 0.05, **c** 0.15, **d** 0.3 and **e** 0.4% Ni dopant; post annealing at 1000 °C



the reusability of the synthesized composites was evaluated by subjecting to photocatalysis for three cycles after subsequent washing with deionized water (Fig. 7c). The degradation efficiency of ZFO composites showed more than 85% reproducibility after three cycles. The observed reduction in efficiency might be due to the material loss during washing steps which could be improved by retrieving from the medium using an external magnetic field.

Figure 8 demonstrated the feasible photocatalytic mechanism of ZFO nanocomposites. When exposed to UV light, ZFO composites absorb enough energy to excite the electrons from valence band (VB) to conduction band (CB), forming free electrons ( $e^-$ ) in CB and holes ( $h^+$ ) in VB [44, 45]. The free electrons may be released into the aqueous solution of dye, which reacts with dissolved oxygen in the

medium to form superoxide radicals ( $\text{O}_2^-$ ). These can further attack water molecules or hydroxyl ions to form reactive hydroxide ions ( $\text{OH}^\cdot$ ); that have the capacity to attack the dye molecules [19, 39]. Meanwhile,  $h^+$  in the valence band can also promote the formation of  $\text{OH}^\cdot$  radicals. Consequently, MB can decompose to nontoxic degradation products such as  $\text{CO}_2$  and  $\text{H}_2\text{O}$ . The resultant changes in the MB solution were also depicted in the figure.

We have compared the photocatalytic efficiency obtained for as-prepared Ni-doped zinc ferrites with other systems used for methylene blue degradation (Table 1). A previous investigation by Jadhav et al. demonstrated the effect of Ni dopant on structural parameters and photocatalytic degradation of Rhodamine B [47]. They found that the photocatalytic effect increases with Ni content

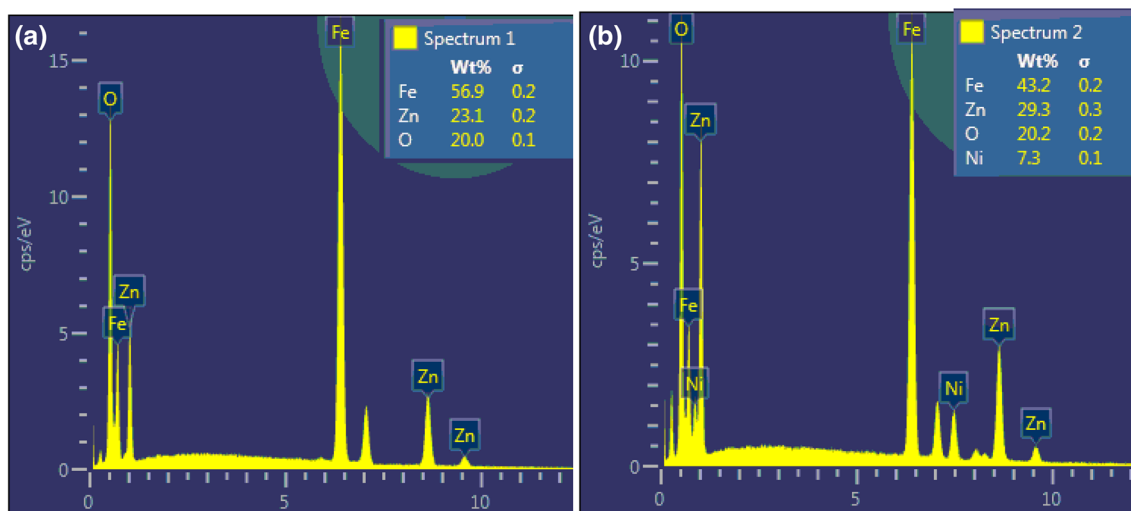
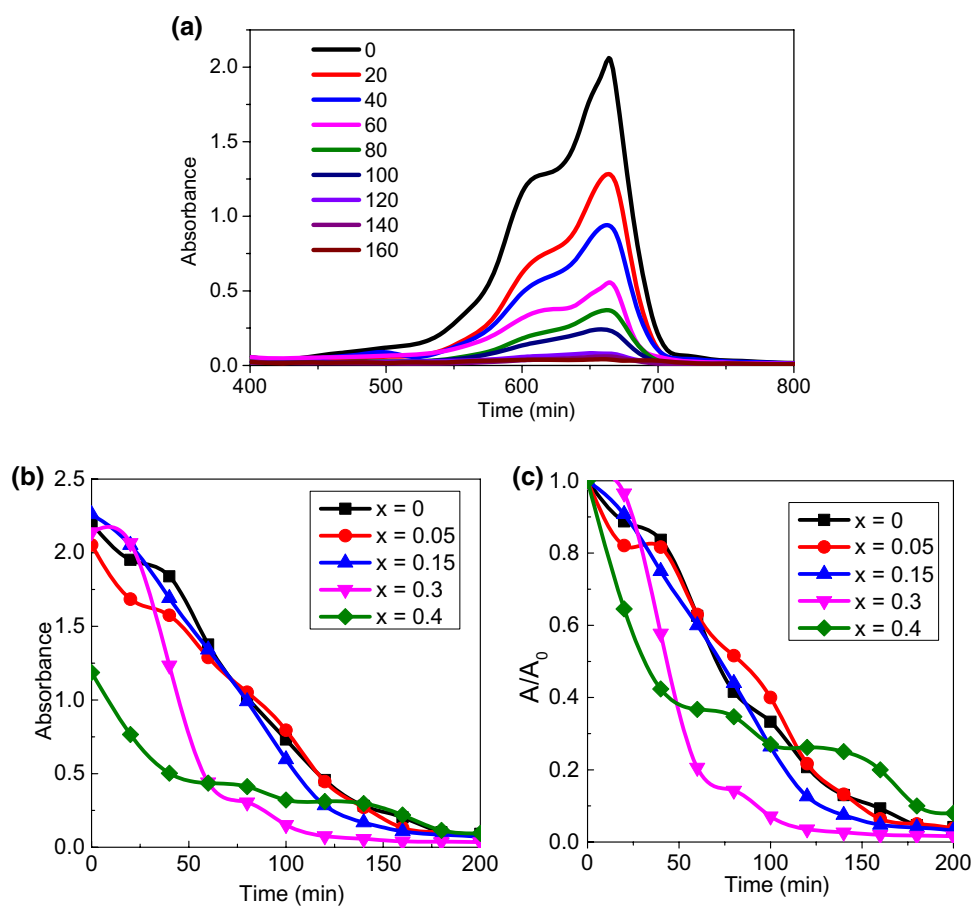


**Fig. 5** EDX spectra of **a** bare zinc ferrites **b** Ni–Zinc ferrites with 30% Ni loading

**Fig. 6** Effect of Ni doping content on the photocatalysis of methylene blue by zinc ferrite nanocomposites annealed at 1000 °C; **a** Absorbance spectra of MB during photocatalysis **b** A plot of absorbance versus irradiation time, **c** plot of ( $A/A_0$ ) versus irradiation time



while using urea as fuel. In the present study, we have investigated the effect of Ni doping on structural and photocatalytic properties of ZFO nanocomposites by using glycine as a green fuel. We observed that the highest photocatalytic activity of 98% was obtained for the optimum

Ni content of 30%. As auto-combustion process parameters could significantly affect the structure and properties of ZFO nanocomposites, the proper correlation between structural features and photocatalytic performance is highly necessitated in this context. The stability of the

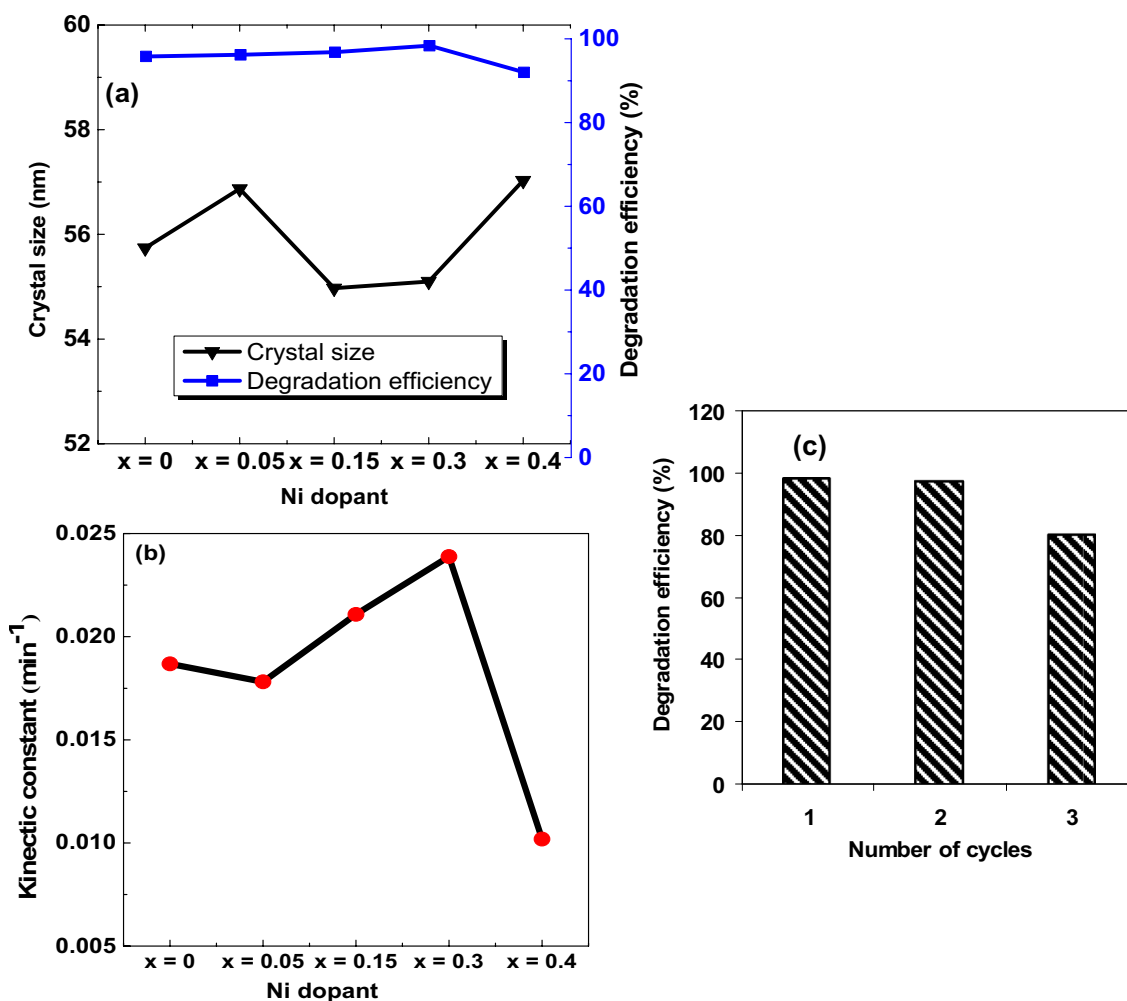


**Fig. 7** Plot showing the variation of crystal size and degradation efficiency with Ni doping, **b** variation of kinetic coefficient of photocatalysis reaction with crystal size, and **c** reusability of synthesized composite Zinc Ferrite Ni-doped 30%

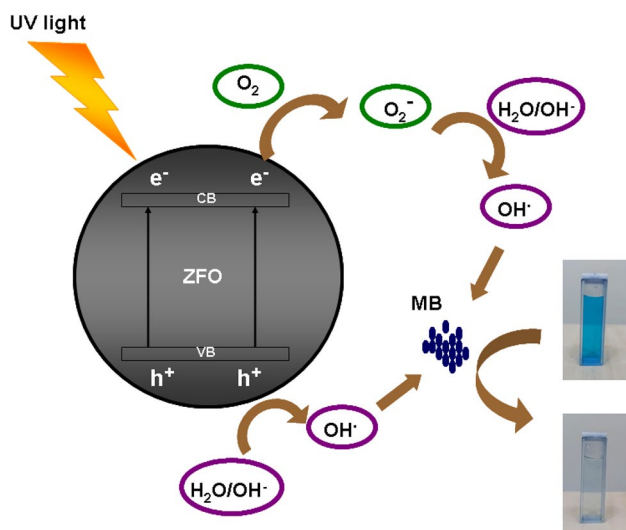


**Fig. 8** The proposed mechanism of photocatalysis of MB solutions using ZFO nanocomposites [46]

material has been proved by doing multiple photocatalysis cycles on the same sample.

## 4 Conclusions

In summary, ZFO nanocomposites with varying Ni dopant were successfully synthesized using auto-combustion followed by the annealing process. XRD revealed the formation of zinc ferrites crystallites with cubic spinel structure. The morphology of different zinc ferrites was evaluated using SEM. The degradation rate of MB solution increases successively with Ni doping up to 30% and thereafter decreases. With an optimum Ni doping (30%), photocatalytic activity up to 98% was achieved with as-synthesized ZFO nanocomposites, which can perform as an environmentally friendly, easily isolable, and recyclable photocatalyst for water treatments.

**Table 1** Comparison of photocatalytic activity of currently investigated ZFO composites with previous reports

| Photocatalyst material                       | Concentration of MB    | Irradiation time (min) | Degradation efficiency (%) | Earlier reports               |
|--|------------------------|------------------------|----------------------------|-------------------------------|
| PANI/Zirconium (IV) silicophosphate          | $1.5 \times 10^{-5}$ M | 120                    | 82                         | Pathania et al. (2014) [8]    |
| Pectin zirconium (IV) selenotungstophosphate | $1.5 \times 10^{-5}$ M | 180                    | 89                         | Gupta et al. (2015) [15]      |
| Zinc ferrites                                | 20 ppm                 | 90                     | 94                         | Padmapriya et al. (2016) [43] |
| Cobalt zinc ferrite                          | 10 mg/L                | 60                     | 77                         | Chahar et al. (2021) [46]     |
| Aluminium zinc ferrites                      | 5 ppm                  | 120                    | 55                         | Gul et al. (2020) [48]        |
| Ni doped Zinc ferrites                       | $2 \times 10^{-5}$ M   | 180                    | 98                         | Present work                  |

**Acknowledgements** This work was supported by the directorate general of scientific research and technological development DGRSDT of Algeria. The authors would like to acknowledge the financial support from the University of Sharjah (Targeted Project Grant No. 2102143096).

## References

- R.B. Baird et al., *Standard Methods for the Examination of Water and Wastewater* (American Public Health Association, Washington DC, 2017).
- G. Muthuraman, T.T. Teng, Extraction and recovery of rhodamine B, methyl violet and methylene blue from industrial wastewater using D2EHPA as an extractant. *J. Ind. Eng. Chem.* **15**(6), 841–846 (2009)
- R.S. Razmara, A. Daneshfar, R. Sahrai, Determination of methylene blue and sunset yellow in wastewater and food samples using salting-out assisted liquid–liquid extraction. *J. Ind. Eng. Chem.* **17**(3), 533–536 (2011)
- S. Li et al., Fast photocatalytic degradation of dyes using low-power laser-fabricated  $\text{Cu}_2\text{O}$ –Cu nanocomposites. *RSC Adv.* **8**(36), 20277–20286 (2018)
- K.M. Lee, S.B.A. Hamid, C.W. Lai, Multivariate analysis of photocatalytic-mineralization of eriochrome black T dye using ZnO catalyst and UV irradiation. *Mater. Sci. Semicond. Process* **39**, 40–48 (2015)
- G. Sharma et al., Guar gum-crosslinked-Soya lecithin nanohydrogel sheets as effective adsorbent for the removal of thiophanate methyl fungicide. *Int. J. Biol. Macromol.* **114**, 295–305 (2018)
- M. Wang et al., Enhanced removal of heavy metals and phosphate in stormwater filtration systems amended with drinking water treatment residual-based granules. *J. Environ. Manag.* **280**, 111645 (2021)
- D. Pathania et al., Fabrication of nanocomposite polyaniline zirconium(IV) silicophosphate for photocatalytic and antimicrobial activity. *J. Alloys Compd.* **588**, 668–675 (2014)
- P.C. Vandevivere, R. Bianchi, W. Verstraete, Treatment and reuse of wastewater from the textile wet-processing industry: review of emerging technologies. *J. Chem. Technol. Biotechnol.* **72**(4), 289–302 (1998)
- Y. Liao et al., Effects of heat treatment scheme on the photocatalytic activity of  $\text{TiO}_2$  nanotube powders derived by a facile electrochemical process. *J. Alloys Compd.* **509**(3), 1054–1059 (2011)
- A. Hajjaji et al., Photocatalytic activity of Cr-doped  $\text{TiO}_2$  nanoparticles deposited on porous multicrystalline silicon films. *Nanoscale Res. Lett.* **9**(1), 1–6 (2014)
- Y. Meor et al., Photocatalytic active nanorutile  $\text{TiO}_2$ : synthesis characterization and photocatalysis tests. *J. Nano Res.* **26**, 17–23 (2014)
- A. Barnasas et al., Growth and characterization of nanostructured Ag–ZnO for application in water purification. *J. Nano Res.* **62**, 75–86 (2020)
- G. Sharma et al., Highly efficient Sr/Ce/activated carbon bimetallic nanocomposite for photoinduced degradation of rhodamine B. *Catal. Today* **33**, 437–451 (2019)
- G. Sharma et al., Preparation, characterization and antimicrobial activity of biopolymer based nanocomposite ion exchanger pectin zirconium (IV) selenotungstophosphate: application for removal of toxic metals. *J. Ind. Eng. Chem.* **20**(6), 4482–4490 (2014)
- B.I. Kharisov, H.R. Dias, O.V. Kharissova, Mini-review: ferrite nanoparticles in the catalysis. *Arab. J. Chem.* **12**(7), 1234–1246 (2019)
- N.M. Mahmoodi, Zinc ferrite nanoparticle as a magnetic catalyst: synthesis and dye degradation. *Mater. Res. Bull.* **48**(10), 4255–4260 (2013)
- H.R. Rajabi et al., Green synthesis of zinc sulfide nanophotocatalysts using aqueous extract of Ficus Johannis plant for efficient photodegradation of some pollutants. *J. Mater. Res. Technol.* **9**(6), 15638–15647 (2020)
- H.R. Rajabi et al., Fast sonochemically-assisted synthesis of pure and doped zinc sulfide quantum dots and their applicability in organic dye removal from aqueous media. *J. Photochem. Photobiol. B* **181**, 98–105 (2018)
- M. Roushani et al., Application of graphene quantum dots as green homogenous nanophotocatalyst in the visible-light-driven photolytic process. *J. Mater. Sci.* **28**, 5135–5143 (2017)
- J.S. Jang, S.J. Hong, J.S. Lee, P.H. Borse, O.S. Jung, T.E. Hong, H.G. Kim, Synthesis of zinc ferrite and its photocatalytic application under visible light. *J. Korean Phys. Soc.* **54**(1), 204–208 (2009)
- P.H. Borse, J.S. Jang, S.J. Hong, J.S. Lee, J.H. Jung, T.E. Hong, H.G. Kim, Photocatalytic hydrogen generation from water-methanol mixtures using nanocrystalline  $\text{ZnFe}_2\text{O}_4$  under visible light irradiation. *J. Korean Phys. Soc.* **55**(4), 1472–1477 (2009)
- J. Ye et al., Photocatalytic simultaneous removal of nitrite and ammonia via a zinc ferrite/activated carbon hybrid catalyst under UV–Visible irradiation. *ACS Omega* **4**(4), 6411–6420 (2019)
- R. Dom, R. Subasri, N.Y. Hebakar, A.S. Chary, P.H. Borse, Synthesis of a hydrogen producing nanocrystalline  $\text{ZnFe}_2\text{O}_4$  visible light photocatalyst using a rapid microwave irradiation method. *RSC Adv.* **2**(33), 12782–12791 (2012)



25. N.D. Raskar et al., One step synthesis of vertically grown Mn-doped ZnO nanorods for photocatalytic application. *J. Mater. Sci.* **30**(11), 10886–10899 (2019)
26. A. Gedanken, et al., Google Patents, Sonochemical coating of textiles with metal oxide nanoparticles for antimicrobial fabrics, 2019
27. Y.I. Kim, D. Kim, C.S. Lee, Synthesis and characterization of CoFe<sub>2</sub>O<sub>4</sub> magnetic nanoparticles prepared by temperature-controlled coprecipitation method. *Phys. B* **337**(1–4), 42–51 (2003)
28. A. Bhosale et al., Influential incorporation of RE metal ion (Dy<sup>3+</sup>) in yttrium iron garnet (YIG) nanoparticles: magnetic, electrical and dielectric behaviour. *Ceram. Int.* **46**(10), 15372–15378 (2020)
29. D. Ponnamma et al., Synthesis, optimization and applications of ZnO/polymer nanocomposites. *Mater. Sci. Eng. C* **98**, 1210–1240 (2019)
30. S. Singamaneni et al., Magnetic nanoparticles: recent advances in synthesis, self-assembly and applications. *J. Mater. Chem.* **21**(42), 16819–16845 (2011)
31. Y. Bao et al., Magnetic nanoparticles: material engineering and emerging applications in lithography and biomedicine. *J. Mater. Sci.* **51**(1), 513–553 (2016)
32. C.-C. Hwang, J.-S. Tsai, T.-H. Huang, Combustion synthesis of Ni–Zn ferrite by using glycine and metal nitrates—Investigations of precursor homogeneity, product reproducibility, and reaction mechanism. *Mater. Chem. Phys.* **93**(2–3), 330–336 (2005)
33. M. Gaidi et al., Enhanced photocatalytic activities of silicon nanowires/graphene oxide nanocomposite: effect of etching parameters. *J. Environ. Sci.* **101**, 123–134 (2020)
34. A. Guinier, *Théorie et technique de la radiocristallographie*. Dunod (1964)
35. W. Meng et al., Photocatalytic activity of highly porous zinc ferrite prepared from a zinc-iron (III)-sulfate layered double hydroxide precursor. *J. Porous Mater.* **11**(2), 97–105 (2004)
36. S. Phumying et al., Nanocrystalline spinel ferrite (MFe<sub>2</sub>O<sub>4</sub>, M=Ni, Co, Mn, Mg, Zn) powders prepared by a simple aloe vera plant-extracted solution hydrothermal route. *Mater. Res. Bull.* **48**, 2060–2065 (2013)
37. R.S. Yadav et al., Structural, magnetic, optical, dielectric, electrical and modulus spectroscopic characteristics of ZnFe<sub>2</sub>O<sub>4</sub> spinel ferrite nanoparticles synthesized via honey-mediated sol-gel combustion method. *J. Phys. Chem. Solids* **110**, 87–99 (2017)
38. M. Rezaei et al., Selective and rapid extraction of piroxicam from water and plasma samples using magnetic imprinted polymeric nanosorbent: synthesis, characterization and application. *Colloids Surf. A* **586**, 124253 (2020)
39. H.M. Rajabi et al., Comparison investigation on photocatalytic activity performance and adsorption efficiency for the removal of cationic dye: quantum dots vs. magnetic nanoparticles. *J. Environ. Chem. Eng.* **4**(3), 2830–2840 (2016)
40. R. Rameshbabu et al., Synthesis and study of structural, morphological and magnetic properties of ZnFe<sub>2</sub>O<sub>4</sub> nanoparticles. *J. Supercond. Novel Magn.* **27**(6), 1499–1502 (2013)
41. A. Lassoued et al., Photocatalytic degradation of methyl orange dye by NiFe<sub>2</sub>O<sub>4</sub> nanoparticles under visible irradiation: effect of varying the synthesis temperature. *J. Mater. Sci. Mater. Electron.* **29**, 7057–7067 (2018)
42. M.M. Naik et al., Green synthesis of zinc ferrite nanoparticles in Limonia acidissima juice: characterization and their application as photocatalytic and antibacterial activities. *Microchem. J.* **146**, 1227–1235 (2019)
43. G. Padmapriya et al., Spinel Ni<sub>x</sub>Zn<sub>1-x</sub>Fe<sub>2</sub>O<sub>4</sub> (0.0 ≤ x ≤ 1.0) nano-photocatalysts: synthesis, characterization and photocatalytic degradation of methylene blue dye. *J. Mol. Struct.* **1119**, 39–47 (2016)
44. P. Dhiman et al., Nano Fe<sub>x</sub>Zn<sub>1-x</sub>O as a tuneable and efficient photocatalyst for solar powered degradation of bisphenol A from aqueous environment. *J. Clean. Prod.* **165**, 1542–1556 (2017)
45. G. Sharma et al., Fabrication and characterization of novel FeO@Guar gum-crosslinked-soya lecithin nanocomposite hydrogel for photocatalytic degradation of methyl violet dye. *Sep. Purif. Technol.* **211**, 895–908 (2019)
46. D. Chahar et al., Photocatalytic activity of cobalt substituted zinc ferrite for the degradation of methylene blue dye under visible light irradiation. *J. Alloys Compd.* **851**, 156878 (2021)
47. S.A. Jadhav et al., Magneto-structural and photocatalytic behavior of mixed Ni–Zn nano-spinel ferrites: visible light-enabled active photodegradation of rhodamine B. *J. Mater. Sci.* **31**, 11352–11365 (2020)
48. S. Gul et al., Al-substituted zinc spinel ferrite nanoparticles: preparation and evaluation of structural, electrical, magnetic and photocatalytic properties. *Ceram. Int.* **46**(9), 14195–14205 (2020)

**Publisher's Note** Springer Nature remains neutral with regard to jurisdictional claims in published maps and institutional affiliations.